ELSEVIER

Contents lists available at ScienceDirect

Materials Science & Engineering A

journal homepage: http://www.elsevier.com/locate/msea





Electro-strengthening of the additively manufactured Ti-6Al-4V alloy

Daudi Waryoba ^{a,*}, Zahabul Islam ^b, Ted Reutzel ^c, Aman Haque ^b

- ^a Engineering, Applied Materials, Penn State University, College Place, DuBois, PA, 15801, USA
- b Mechanical & Nuclear Engineering, Penn State University, University Park, PA, 16802, USA
- ^c Applied Research Laboratory, Penn State University, University Park, PA, 16802, USA

ARTICLE INFO

Keywords: Electric current processing Nanohardness Electron backscattered diffraction (EBSD) Transmission electron microscopy (TEM) Schmid factor Taylor factor

ABSTRACT

Structure-property-processing relationship has been studied in additively manufactured Ti–6Al–4V alloy. The processing was performed using in-situ electron microscope (EM) at a moderate current density of 5×10^5 A/cm² applied for 5 min, and by suppressing Joule heating with massive heat sinks such that the temperature rise was <180 °C and the mechanical properties were not compromised. The results show that while the grain size increased by ~15%, the nanohardness increased by 16%. This is attributed to the pronounced dislocation generation, regeneration, and clustering as well as defect healing. Ultimately, there is a reduction in the residual strain and a significant increase in the intrinsic strength as evidenced by the high Taylor factor of the electric current processed specimen. This novel processing technique represents an alternative pathway for active controlling of microstructure and internal defects for parts that might be sensitive to high-temperature processing or conventional methods.

1. Introduction

Microstructures formed in the additive manufacturing (AM) process are governed by a complex combination of processing parameters, which include the heat input of the energy source, scan rate, deposition rate, and the dwell time between individual layers [1,2]. Consequently, reported mechanical properties [3,4] of AM parts show large scatter and inconsistency largely due to many complex interactions between the fabrication conditions which result to a wide range of microstructural parameters. Among the range of materials commonly used in AM processes, titanium alloys, especially Ti-6Al-4V, have received considerable attention because of their applications in aerospace and biomedical industries [5-7]. Ti-6Al-4V alloy is the most studied material in AM processing due to its high corrosion resistance and high specific strength [8]. However, the ultimate tensile strength, elongation, Young's modulus and fatigue performance of additively manufactured Ti-6Al-4V alloy have been reported to be negatively affected by internal defects [9,10]. Likewise, the spatial distribution of these defects creates unwanted anisotropy of tensile properties [11,12]. In order to ensure that additively manufactured Ti-6Al-4V products meet the quality standards required for applications in critical areas such as in aerospace and biomedical, internal defects ought to be reduced/eliminated for improvement of the mechanical properties.

Due to the high solidification front velocity in AM, which can be as high as ~ 10 mm/s [13], on cooling below the β -transus temperature of Ti-6Al-4V, $\beta \rightarrow \alpha$ diffusional transformation develops a variety of microstructure and texture that depends on the cooling rate. Typical microstructures in as-built AM Ti-6Al-4V materials are dominated at the macro-scale by columnar prior β-grains that are aligned with the build direction [14–16]. Within these columnar prior β -grains, a mixture of basketweave or colony α -laths, acicular α' (martensite), and retained β phases is present [14-16]. In particular, laser AM Ti-6Al-4V is characterized by columnar grains with fine acicular α or α' laths (martensite) as a result of the high cooling rates and low heat input [3,15]. Both the size and fraction of the α -laths, acicular α' , and size of β grains determine the mechanical properties. Aside from these microstructural parameters, internal macro- and microscopic defects have also shown to significantly affect the mechanical properties. Microscopic defects include micropores, residual/transformation stresses, and microstructural defects such as grain boundary cracking and non-equilibrium microstructures due to intrinsically high-solidification rate of the process [17,18]. On the other hand, macroscopic defects include pores and cracks due to lack of fusion, volumetric shrinkage, entrapped gases, and voids caused by lack of melt pool overlap [19,20]. Porosity is a common defect in metal AM parts and currently, the most acceptable post-processing technique to mitigate its effects is to apply hot-isostatic pressing (HIP). HIP is often

E-mail address: drw29@psu.edu (D. Waryoba).

^{*} Corresponding author.

applied to AM structures in order to "heal" process-related voids and pores within the builds. For AM Ti–6Al–4V, HIP is usually performed at $\sim\!900\,^\circ\text{C}$ and 100 MPa for 2 h in an argon atmosphere [21,22]. However, the application of this post-processing treatment has been shown to coarsen the microstructure and decrease the strength of AM materials [21]. Heat-treatment is another post-processing method that is used for stress relieving and microstructural modification/enhancement of AM parts [2,23,24]. However, high temperature annealing that is typically used for optimizing the microstructure of AM parts results in a deterioration in mechanical properties due to thermally activated processes such as recovery, recrystallization, and grain growth.

In this paper we are presenting a unique method of alleviating microstructural internal defects, by room-temperature electric current processing. The method uses high electron wind drift to promote an enhanced electron-defect interaction that produce high dislocation density as well as annihilation of microstructural defects without compromising the mechanical properties. Earlier studies on the use of high density electric current or electropulsing for material processing include electromigration [25-27], and the electro-plasticity [28,29] in metals. Depending on materials and processing parameters, electropulsing can be used for improving formability of materials [28,29] or induce recrystallization [30,31] by exploiting resistive (Joule) heating. However, recently this technique has been shown to produce comparable microstructure and properties to that of conventional annealing at a very short duration and a relatively low temperature [32,33]. This has been attributed largely to an athermal effect, rather than the thermal component (Joule heating). The enhanced athermal effect, due to electron-wind (electron-defect interaction) momentum transfer, promotes intensive vacancy diffusion/atomic flux at localized strained areas such as lattice defects and grain boundaries [34,35]. Besides formability and annealing, several authors [36,37] have used electric current processing/electropulsing to promote phase transformation in alloys. For example, Wang et al. [38] working on electric pulse heat treatment of modified titanium alloy Ti-6Al-4V-4Zr-Mo reported formation of nano-sized lath-shaped $TiAl_3$ precipitates within α plates. The mechanism for the formation of these precipitates was attributed to the migrational motion of Al-atoms induced by the electric current. Similarly, Pan et al. [39] observed electric current-induced segregation of carbon in the near-surface regions of the Fe-0.45C-0.27Si-0.44Mn steel. This segregation behavior of metastable carbon atoms in the martensite was activated by the applied high current density.

Electric current processing/electropulsing has also been used to develop "current-oriented" microstructures. In fabricating steel wires, Qin and co-workers [40] used electropulsing to develop nanostructured lamellae that were aligned almost parallel to the electric current direction. They noted that lamellae that are perpendicular to the electric current direction were easier to transform into grain structures than the parallel ones. Other researchers have also used electropulsing to heal cracks [41,42]. A comprehensive review on the application of electric current processing/electropulsing for improving the performance of metallic materials is presented by Sheng et al. [43].

Our investigation on the use of electric current processing for alleviating microstructural internal defects was done on powder bed fusion additively manufactured Ti–6Al–4V alloy using a dc electric current density below electromigration failure limit (i.e., $<\!10^6~\mathrm{A/cm^2})$ to avoid degradation in mechanical properties [44]. Characterization was performed using optical microscopy, electron backscatter diffraction (EBSD), transmission electron microscopy (TEM), and nanohardness techniques to quantify the benefit.

2. Experimental procedures

The as-built test coupons were supplied by Penn State's Center for Innovation Material Processing thru Direct Digital Deposition (CIMP-3D). The samples were produced using an EOS M280 Laser-Powder Bed Fusion machine. The material feedstock for the build was EOS *Titanium*

Ti64 (which conforms to ASTM B348 Grade 23 powder material specifications), with particle size ranging between 15 μm and 45 μm. The standard EOS Ti–6Al–4V exposure parameters for processing 60 μm layers, referred to as $Ti64_060_110$ Speed, was employed.

Specimens for microstructural characterization were prepared by grinding with SiC paper up to a P2000 grit size and polishing with 3 μm diamond slurry. Final polishing was done on a vibratory polisher for at least 2 h with a chemical-mechanical polishing slurry consisting of 0.05 μm alumina-silica. For optical micrography, specimens were etched with Kroll's reagent. This is a standard micro-etchant solution consisting of 1.5 mL HF, 4 mL KNO3, and 94 mL of H2O. ASTM E112 – 13, Standard Test Methods for Determining Average Grain Size, was used to determine the average grain sizes.

Electro-strengthening was performed at low temperature using electric current processing at a current density of $5\times10^5~\text{A/cm}^2$. A custom stage with electrical biasing capability was built to perform this experiment. To ensure the sample remains close to room temperature during processing, a non-conductive massive heat sink was attached to the sample as shown in Fig. 1a. The temperature of the specimen during electric current processing was recorded by infrared thermal imaging as shown in Fig. 1b. The maximum temperature recorded was below 180 °C, which is significantly far below the processing temperature for HIP (~900 °C). By removing the Joule heating due to electrical current flow, we ensure that the electron wind force remain the dominant factor [32]. This is the atomic scale force that is imparted on only defects, by the momentum change in electrons.

During the experiment, we gradually increased the current density in a series of steps, and we continuously monitored the resistance change of the sample. The current was increased by 0.1 A per step, and the sample was checked after every current step using optical microscope to observe any discernible microstructure change.

EBSD data acquisition was performed in a Helios 661 NanoLab FEI dual beam field emission scanning electron microscope (FE SEM) using Aztec EBSD Nanoanalysis software, ver. 4.2 (Oxford Instruments). Scanning was done at a step size of 0.1 μm , and a minimum of 3 randomly selected scans were acquired for each specimen. All EBSD analyses were done using CHANNEL 5 software (ver. 5.12.57.0). In order to avoid spurious boundaries, the minimum boundary misorientation was set to 2°. Grain and α -lath boundaries were marked using a threshold of 10° .

In-situ TEM experiment was used to record progression of the microstructure evolution during electric current processing. TEM was performed inside a FEITM Talos F200X scanning/transmission electron microscope (S/TEM) with a resolution of 0.12 nm using field emission gun and 200 kV acceleration voltage. In-situ TEM enables real-time high-resolution imaging as well as electron diffraction. In a typical experiment, we first bias the specimen while measuring the current. About 2 min of time interval is allowed between each 0.2 A DC current step increments to discern the ensuing microstructural changes by observing bright field (BF) images and the corresponding diffraction patterns. When the current density reached $5\times10^5~\rm A/cm^2$, we noticed discernible microstructure changes within 5 min of biasing.

Nano-hardness of the as-received and electric current processed specimens was evaluated using a CSM Instruments nanoindenter with the Berkovich diamond tip [45] based on the Oliver and Pharr approach [46] and ISO 14577 standard for measurements.

3. Results

It is clear from the optical micrographs in Fig. 2 that the microstructures of the as-built and electric current processed specimens were dominated by the fine basketweave α/α' (martensite) lath structure. The average grain sizes were $143.9\pm41.4~\mu m$ and $165.8\pm33.4~\mu m$, for the as-built and electric current processed specimens, respectively. In other words, the grain size increased by 15.2% after electric current processing.

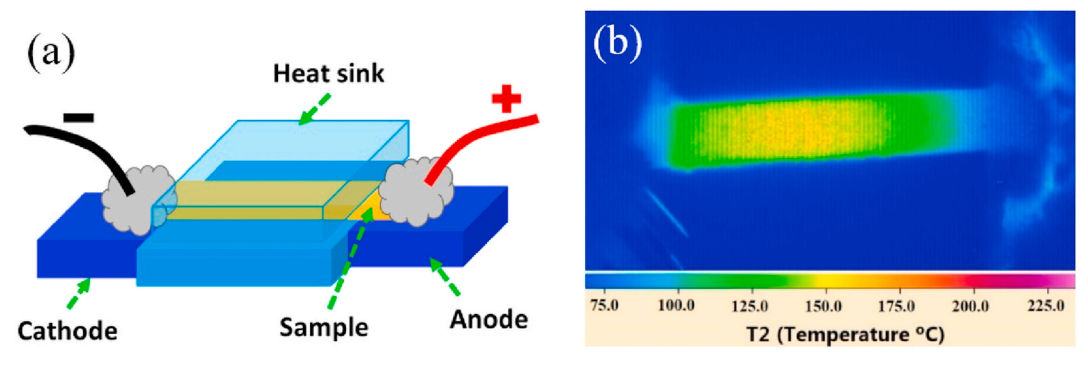


Fig. 1. (a) Schematic showing set-up and (b) thermal image showing the temperature distribution in the Ti-6Al-4V alloy during electric current processing.

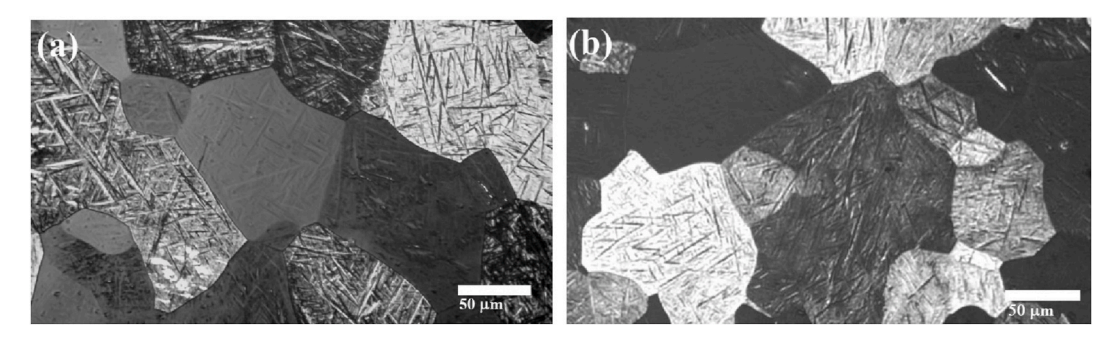


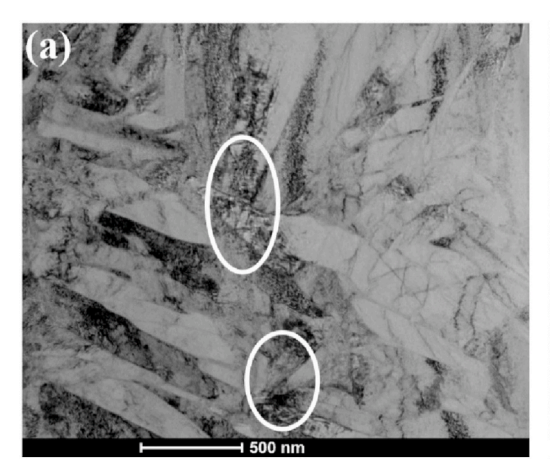
Fig. 2. Optical micrographs of Ti-6Al-4V specimens in the (a) as-built, and (b) electric current processed conditions.

Our in-situ TEM study showed discernible microstructural changes during the electric current processing as shown in Fig. 3, where defects in the α/α' -laths in the as-built specimen (Fig. 3a) were either annihilated or transformed to dislocation clusters/pileups (as shown by white arrows and ellipses in Fig. 3b). A comparison between Fig. 3a and b indicates a significant amount of dislocation pileup as indicated by white arrows in Fig. 3b. Additionally, we noticed α -laths reconstruction as indicated by white ellipses. The top elliptical area in Fig. 3b indicates the reconstruction of α -laths by annihilating dislocations, whereas the bottom elliptical area indicates dislocation accumulation and clustering.

Fig. 4a and b shows TEM micrographs of the microstructure of Ti–6Al–4V alloy in the as-built condition and after electric current processing, respectively. We have compared the same area of interest before and after the application of electric current as shown in Fig. 4a and b by cyan color dotted circles. As-built specimen does not contain any twins as shown in Fig. 4a. However, upon the application of the

electric current, we noticed twin formation due to the electron wind force (EWF) effects as shown by yellow-colored arrows in Fig. 4b. Fig. 4c shows a magnified view of the newly formed twin as indicated by the yellow colored rectangular dotted area in Fig. 4b. Selected area electron diffraction (SAED) pattern of as-received sample is shown in Fig. 4d which clearly indicates the polycrystalline nature of the sample, whereas Fig. 4e indicates SAED pattern of electric current processed sample. The presence of double spots (yellow color dotted elliptical areas in Fig. 4e) is an indication of twin formation in the sample. This twin formation might contribute to the enhancement of the hardness of the sample after annealing as described in the following sections.

The mechanical behavior of the specimen before and after electric current processing was evaluated by the nanohardness test as shown in Fig. 5 and Table 1. The hardness increased from about 5 GPa to \sim 6 GPa after electric current processing. This is an appreciable increase of about 16%. It is well-known that hardness and toughness (plastic work) are



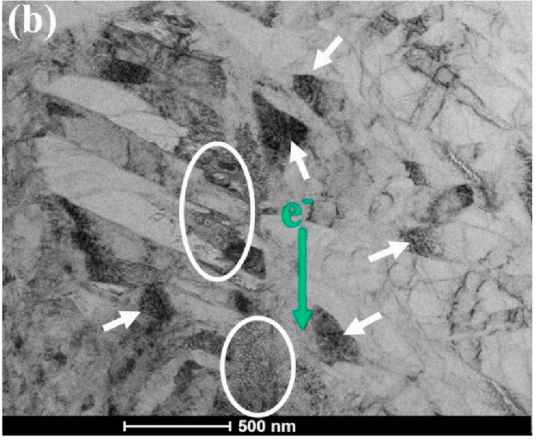


Fig. 3. TEM micrographs of Ti-6Al-4V alloy showing defects at a location near the edge of the sample: (a) before electric current processing and (b) after applying a current density of 5×10^5 A/cm². The arrows and ellipses show dislocation accumulation, clustering, and annihilation.

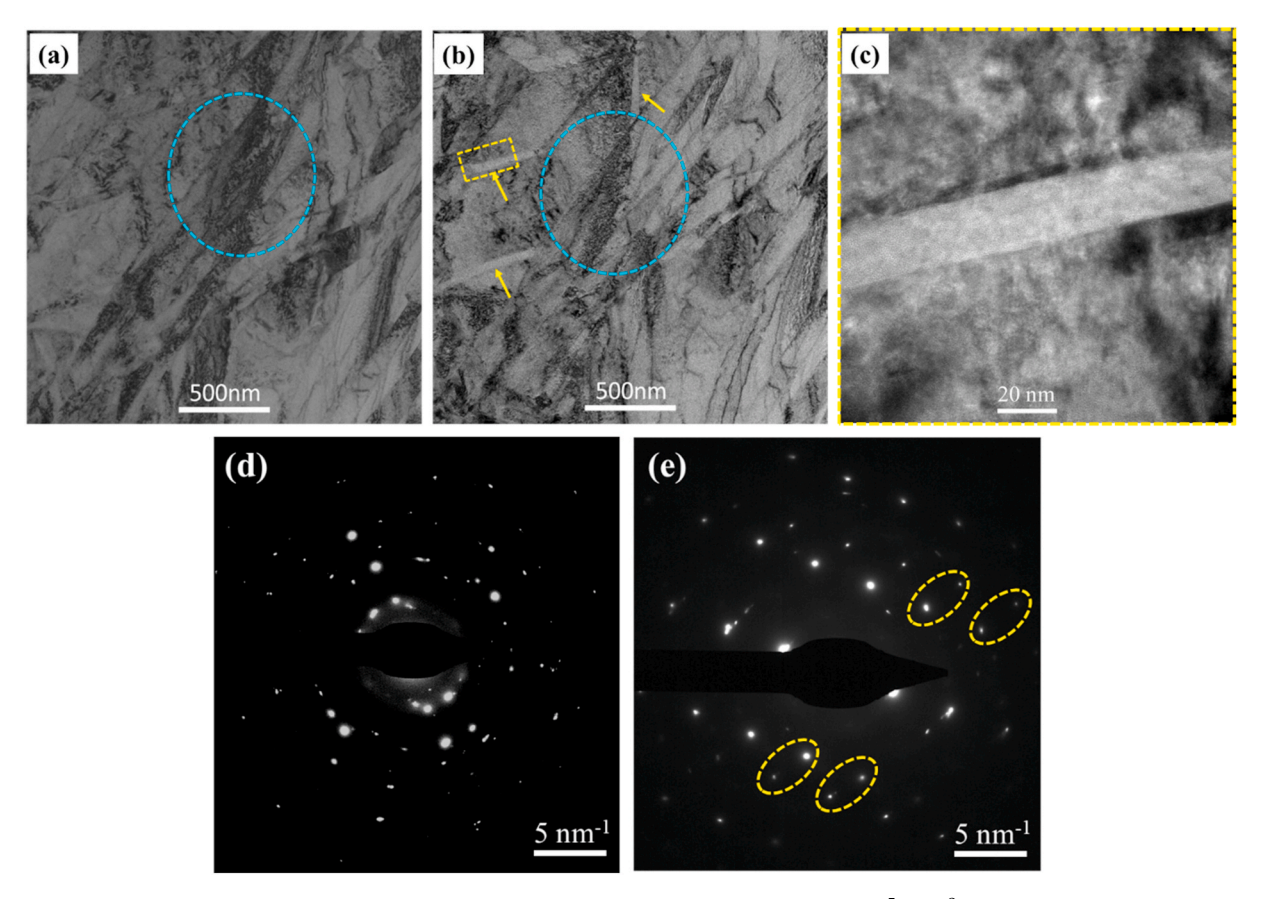


Fig. 4. TEM micrographs of Ti-6Al-4V alloy: (a) as-built specimen, (b) after applying a current density of 5×10^5 A/cm², (c) twin formation, (d) SAED pattern of as-received sample, and (e) SAED pattern after a current density of 5×10^5 A/cm².

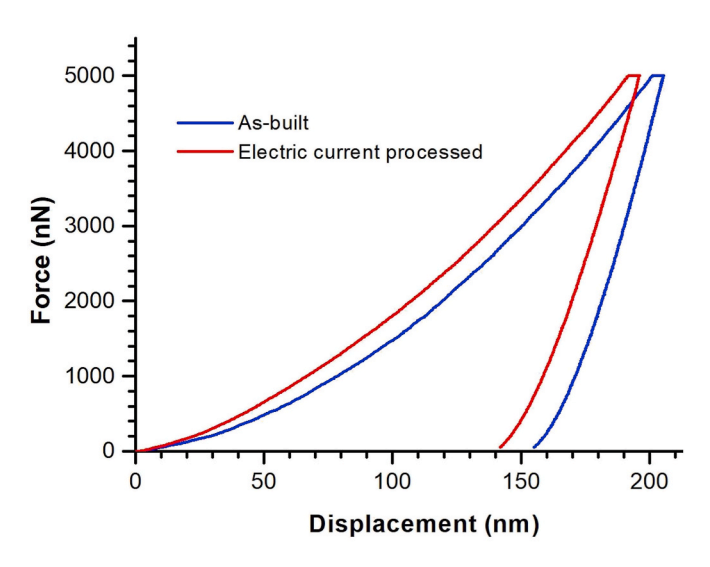


Fig. 5. Load-depth indentation curves for Ti–6Al–4V specimens in the as-built and after electric current processing conditions.

Table 1
Nanohardness, plastic work ratio, and elastic modulus for Ti–6Al–4V.

Condition	Nano-hardness (GPa)	Ratio of plastic work to total work	Young's Modulus (GPa)
As-built	5.431 ± 0.344	0.729	134.7
Electric current processed	6.300 ± 0.240	0.705	128.9
% change	+16%	-3%	-4.3%

mutually exclusive. Our results are therefore remarkable because the 16% increase in hardness is achieved at the expense of only 3% decrease in the plastic work. We also calculated the elastic modulus from the indentation curve shown in Fig. 5 based on the Oliver and Pharr approach [46]. The values of the elastic modulus, as summarized in Table 1, were 134.7 GPa and 128.9 GPa for as-built and electric current processed specimens, respectively.

We also used electron backscatter diffraction (EBSD) to evaluate microstructural changes that can be related to the hardness. In this case, we performed a detail analysis of the Taylor factor/Schmid factors on specimens before and after electric current processing. In hexagonal close packed (hcp) metals, there are 24 possible slip systems that include 3 basal slip $\{0001\}<11\overline{2}0>$, 3 prismatic slip $\{1\overline{1}00\}<11\overline{2}0>$, 6 pyramidal $\langle a \rangle$ slip $\{1\overline{1}01\}\langle 11\overline{2}0 \rangle$, and 12 pyramidal $\langle a + c \rangle$ slip $\{10\overline{1}1\}<11\overline{23}>$ systems [47,48]. However, there is a consensus that prismatic slip is easier to activate than basal, and that basal slip is more easily activated than pyramidal slip [47,49,50]. Pyramidal slip system is very resistant to slip, and its critical resolved shear stress (CRSS) is reported to be about 7 times higher than that of basal slip system [47,51]. It can also be argued that the $\langle c + a \rangle$ slips have Burgers vectors that are significantly longer than for the <a> slips and hence are energetically less favored and tend to have higher resistance to motion. For this reason, pyramidal slip system was omitted in this study.

Fig. 6 shows representative Schmid factor maps for basal slip system before and after electric current processing. It is clear that both microstructures exhibit a basketweave α lath structure. The widths of the α laths were determined to be $0.46\pm0.41~\mu m$ and $0.53\pm0.47~\mu m$ for the as-built and electric current processed specimens, respectively. It is interesting to note that the width increased by the same amount of 15.2% as that of the grain size.

The Schmid factor maps for basal slip system show a distinctive

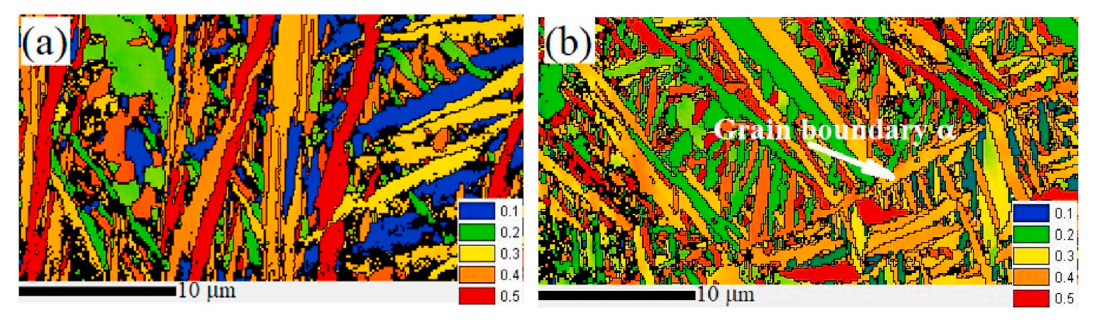


Fig. 6. Basal Schmid factor maps for the Ti6Al4V specimens in the (a) as-built, and (b) electric current processed conditions.

change in Schmid factors from high in the as-built specimen to low in electric current processed specimen. The corresponding Taylor factors are presented in Fig. 7, and they clearly show higher values of Taylor factors for electric current processed specimen than for as-built specimen.

4. Discussion

Most of the electric current-induced phenomena reported in the literatures used high current density in the order of $10^6~{\rm A/cm^2}$. The high current density was intended to induce recrystallization and grain growth, which is often accompanied with a reduction in the microhardness [52]. On the contrary, in this investigation we used low current density, ten times lower than what is reported in the literature, to heal the microstructure while limiting grain growth. The thermal image in Fig. 1b, taken during application of the current, shows that the temperature was also maintained below 180 °C, thereby keeping Joule heating to a minimum.

Using in-situ TEM (Figs. 3 and 4) we have demonstrated that high electron-wind force (athermal effects) can transform defects such as micro/nano cracks and micropores, in the as-built specimen, to dislocation pileups, loops, and clusters. As illustrated in Fig. 8, the electron wind force provides enough stress field to pull dislocations towards the defect, and since defects are dislocation sinks this result into either dislocation pileups and clustering, dislocations loops, or annihilation. The dislocation pileups at the defect can also generate sufficient stress field to emit other dislocations, i.e. become sources of dislocations, or with the combined effect of the Joule heating, can cause dislocation climb. Arguably, besides electron-dislocation interaction, this dense

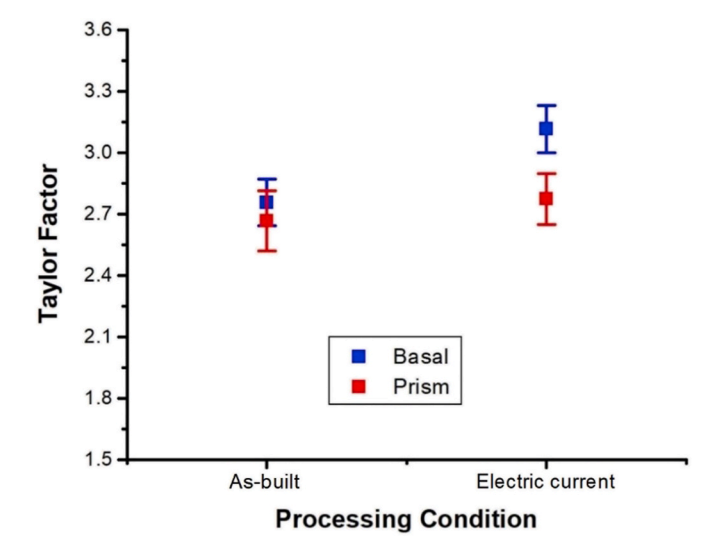


Fig. 7. Taylor factors for the Ti6Al4V specimens in the as-built and electric current processed conditions.

network of mobile dislocations would also enhance dislocation-dislocation interaction resulting to jogs and kinks, annihilation, as well as creating immobile/forest dislocations (sessiles). It is well documented and agreeable that dislocation pileups, sessiles, jogs, and kinks provide resistant to yielding, and contribute to increase in the flow stress

We can deduce that the increase in the hardness can be attributed to the so-called "dislocation source limited strengthening" mechanism [53, 54]. In this mechanism, it is envisioned that the high electron wind force draws the dislocations from the vicinity and towards the free surfaces of the defects. Some of these dislocations are annihilated thereby lowering the stored elastic energy [55], whereas some become more resistant to yield [56]. Consequently, the material become more resistance to deformation, i.e. there is a corresponding increase in the hardness and flow stress. This phenomenon is similar to the defect healing and strengthening by cycling loading as reported by Wang et al. [57].

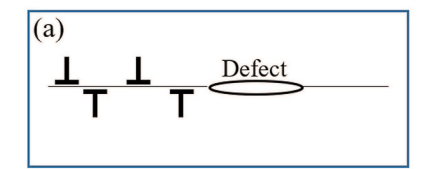
We also analyzed residual strain in the two specimens through measurement of local variations/spread in lattice orientations or Kernel Average Misorientation (KAM) [58,59]. This analysis is done for every pixel in a kernel, provided that the misorientation does not exceed a predefined threshold value, e.g. 5° in this study. The threshold is used to exclude well-defined grain boundaries in the analysis. KAM correlates well with macroscopic plastic strain and is used to highlight regions of high residual strain [58,59]. The higher the residual strain, the higher the KAM value, and vice versa for low residual strain.

Fig. 9 shows the Kernel Average Misorientation (KAM) maps for the microstructure of the as-received material (Fig. 9a) and after electric current processing (Fig. 9b). The legend scale in Fig. 9 shows misorientations between neighboring points for the 2nd nearest-neighbor kernel within a predefined threshold of 5°. The lower the scale, the lower the residual strain. There is a clear evidence of the reduction/elimination of residual strain via electric current processing. This may be a very important result, since the additive manufacturing process is known to generate significant residual stress.

To investigate the dislocation interaction and annihilation mechanism under electron wind force (EWF), we developed computational models using molecular dynamics (MD) simulation. The details of the simulation have been described elsewhere [32,60]. The models can predict the microstructure for various intensities of stress, current, and temperature which can be an efficient path towards optimizing the new process by avoiding combinatorial experiments. The molecular dynamic (MD) simulations were performed by LAMMPS [61] package using an embedded atom method (EAM) [62] developed for Ti–Al system [63]. Functional form of EAM potential is written as follows:

$$\begin{split} E_{EAM} &= \sum_{i=1}^{N} F_{i}(\overline{\rho}_{i}) + \ \frac{1}{2} \sum_{i=1}^{N} \ \sum_{i \neq j}^{N} \mathcal{Q}_{ij} \big(r_{ij} \big) \\ \overline{\rho}_{i} &= \sum_{j=1, \ j \neq i}^{N} \rho_{i} \big(r_{ij} \big) \end{split} \tag{1}$$

where, E_{EAM} , F_i , $\overline{\rho}_i$, \emptyset_{ij} are the system total energy, embedded energy as a



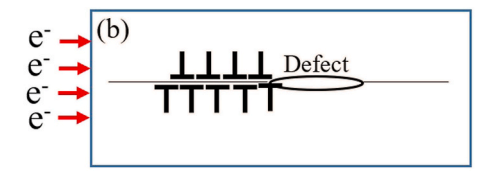


Fig. 8. Illustration of dislocations in the as-built sample (a) and dislocation clustering after electric current processing (b).

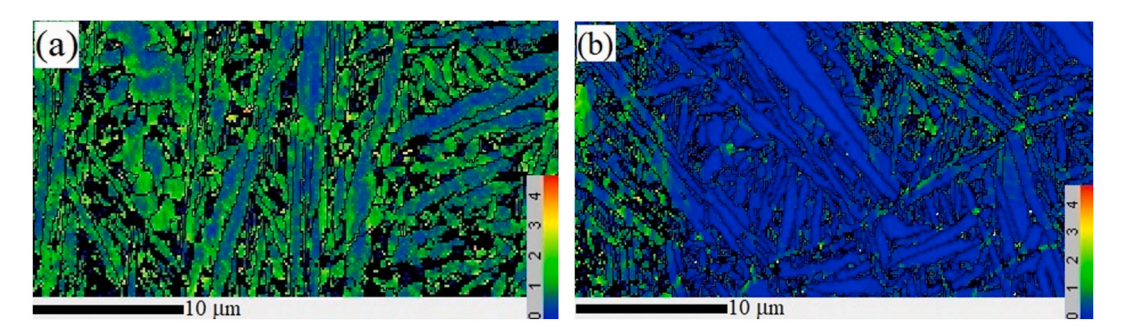


Fig. 9. KAM maps for the Ti6Al4V specimens in the (a) as-built and (b) electric current processed conditions. A threshold of 5° was used to exclude well-defined grain boundaries in the analysis.

function of electron density, host electron density and pair potential as a function of distance rii between two atoms i and j, respectively. In our present study, we used Voronoi tessellation method to model polycrystalline specimens with hexagonal closed packed structure of titanium (Ti) with a lattice constant of a = 2.95 Å and c = 4.68 Å. The total number of grains were 10 and the mean grain size was approximately 8 nm. After building the polycrystalline sample we replaced 6% Ti atoms by aluminum (Al) atoms. Afterwards, we checked the polycrystalline Ti alloy sample to avoid overlapping of atoms at the grain boundaries (GBs). Then we optimize the sample using conjugate-gradient (CG) energy minimization method followed by several thousand steps NPT dynamics with a time step of 0.5 fs. In our present study, we model the electrical current effects by applying an equivalent wind force on individual atoms, obtained from the Huntington-Grone model [64]. Total electrical processing simulation was conducted for 500 ps at 400 K. Fig. 10a and b shows the sample before and after processing. Dotted yellow color arrowhead compares the same area on the pre and post-processed samples. From Fig. 10b it is evident that EWF significantly reduces dislocations in the sample which further facilities grain growth in the sample. Initially, we started with 10 numbers of grains which reduces to 3 numbers of grains due to the dislocation annihilation. In Figs. 10c and d we have tracked individual dislocations by hiding atoms which also indicates a significant amount of dislocation reduction in the sample. In our present study, we have also tracked total dislocations density to gain quantitative insights on the dislocation annihilation as shown in Fig. 10e. Results indicate that almost one order of magnitude dislocation density annihilation after processing which supports the KAM analysis in Fig. 9.

Another interesting phenomenon in this work is the pronounced growth of the twins due to the high electron wind force as indicated earlier in section 3 (Fig. 4). It should be noted that, to the best of our knowledge, this is the first time that in-situ TEM is used to show real-time growth of twin structures due to electric current processing. Obviously, the growth of the twin structures would unquestionably increase the resistance to dislocation motion, and subsequently contribute to the increase in the hardness and flow stress.

The dominant deformation mode at room temperature in HCP metals is dislocation slip in the basal $\{0001\}<11\overline{2}0>$ and prismatic slip $\{1\overline{1}00\}<11\overline{2}0>$ systems [65,66]. But basal and prism slip systems do not provide five independent slip systems that are required to satisfy the von Mises' compatibility criterion. Consequently, pyramidal < a + c>

slip system and twinning provide the additional requirement for the plasticity of these metals. However, pyramidal <a + c> slip system is unfavorable due to its high critical resolved shear stress (CRSS), and thus twinning becomes the energetically favorable deformation mode especially during low-temperature or high-strain rate deformation. Electropulsing is considered to be a high-strain rate micro-deformation.

Twinning occurs by dissociation of a basal <a> dislocation into twinning dislocations associated with $\{1\overline{1}02\}$ twins at sites or interfaces with high local strain such as pileups and α/β interfaces. The dissociation of the basal <a> dislocations with a Burgers vector $\mathbf{b} = \frac{1}{3} < 11\overline{2}0 >$ into twinning dislocations can be represented with successive reactions of the form [66].

where \boldsymbol{b}_{T}^{0} and \boldsymbol{b}_{T}^{1} are immobile residual dislocations, $\boldsymbol{b}_{t}^{(1011)} = \frac{4\kappa^{2}-9}{3+4\kappa^{2}} < 11\overline{2}0 >$ is primary twin, $\boldsymbol{b}_{t}^{(1012)} = \frac{3-\kappa^{2}}{3+\kappa^{2}} < 10\overline{1}1 >$ is secondary twin, and $\kappa = \frac{c}{a}$ ratio. For Ti–6Al–4V alloy, the lattice parameter a = 2.95 Å and c = 4.68 Å [67]. Thus, the magnitude of the Burgers vector for secondary twin dislocation is

$$b_t = \left| \boldsymbol{b}_t^{(1012)} \right| = \frac{3a^2 - c^2}{\sqrt{3a^2 + c^2}} = 0.6 \text{ Å}$$
 (3)

It is noted in Fig. 4b that upon applying a current density of 5×10^5 A/cm², the dislocation pileups at the front of the twin were swept with the front and allowed the appreciable twin growth. This can be explained by considering the drag force on dislocations due to electron wind force. This force can be expressed using the Peach-Koehler [68] Eq. (4)

$$F = (\sigma.b) \wedge l \tag{4}$$

where F is the drag force, σ is the local stress field, b is the Burgers vector, and l is the dislocation line vector. For edge dislocation where the Burgers vector is perpendicular to the dislocation line vector, Eq. (4) is reduced to

$$F = \tau b \tag{5}$$

where τ is the shear stress due to the drag force and b is the magnitude of the Burgers vector. Slip or twinning occurs when $\tau = \tau_{CRSS}$, the critical

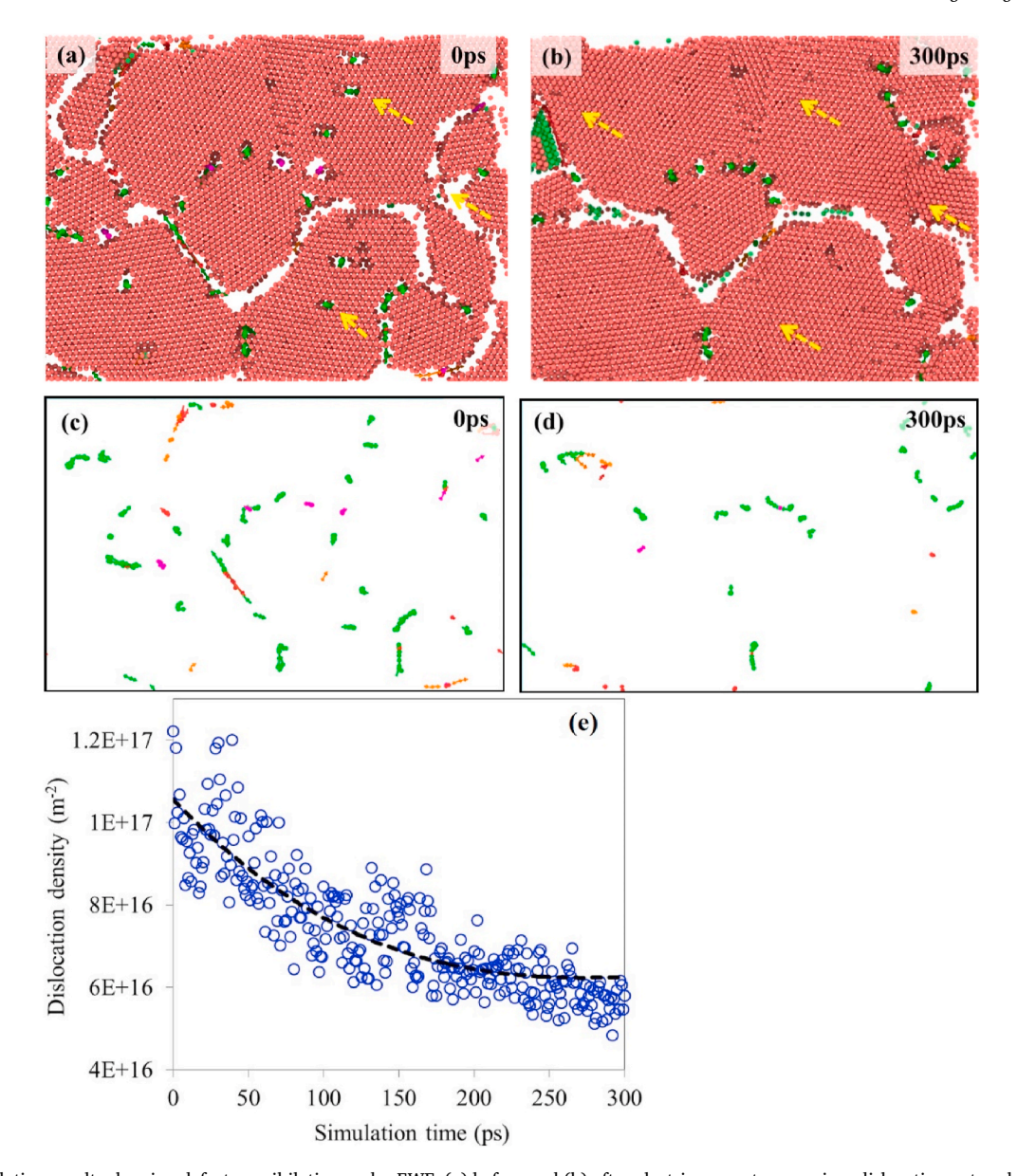


Fig. 10. MD simulation results showing defects annihilation under EWF: (a) before and (b) after electric current processing; dislocation network: (c) before and (d) after processing, and (e) total dislocation density generated during processing.

resolved shear stress for slip or twinning.

The critical resolved shear stress, τ_{CRSS} , for Ti–6Al–4V is about 300–400 MPa for basal and prismatic slips [47] and assumed to be the same for twinning. Using $\left| \boldsymbol{b}_t^{(1012)} \right| = 0.6$ Å, the critical shear drag force (i. e. minimum shear force to initiate dislocation motion) per unit length of dislocation is

$$F_{CSFs}^{t} = \tau_{CRSS}b_{t} = 400 \times 10^{6} (6 \times 10^{-11}) \text{ N} / \text{m} = 2.40 \times 10^{-2} \text{ N} / \text{m}$$
 (6)

If one considers slip in the basal and prism systems, these systems have <a> dislocations with a Burgers vector $\boldsymbol{b}=\frac{1}{3}<11\overline{2}0>$, and magnitude of $|\boldsymbol{b}|=a$. The corresponding critical shear drag force per unit length of dislocation is

$$F_{CSFs}^{s} = \tau_{CRSS}b = 400 \times 10^{6} (2.95 \times 10^{-10}) \text{ N/m} = 1.18 \times 10^{-1} \text{ N/m}$$
 (7)

On the other hand, electron wind force is due to the interactions between drifting free electrons (electron gas/cloud) and defects such as dislocations. From quantum dislocation mechanics [28,69], the magnitude of the electron wind force depends on the orientation between the

Burgers vector and the direction of the current vector. Also, based on the principle of virtual work, the direction of the electron wind force should be normal to the shear slip vector at the point of interest. Thus, considering specific electrical resistivity due to dislocations, the electron wind force per unit length of dislocation can be expressed as [65,66]:

$$\boldsymbol{F}_{wind} = \frac{\rho_d}{N_d} e n_e \left(\frac{\boldsymbol{j.b}}{|\boldsymbol{b}|} \right) \left(\frac{\boldsymbol{m} \times \boldsymbol{n}}{|\boldsymbol{m} \times \boldsymbol{n}|} \right)$$
(8)

Where j is the current density vector, m is shear slip vector, n is slip normal vector, ρ_d is electrical resistivity due to dislocations, N_d is the mobile dislocation density, e is electron charge, and n_e is electron density/concentration expressed as

$$n_e = \frac{\rho N_A Z^*}{W} \tag{9}$$

where ρ is the density, W is the atomic weight, N_A is the Avogadro number (=6.022 \times 10²³ atoms/mol), and Z^* is effective valence number.

For the case where the current vector is in the same direction as the

Burgers vector, Eq. (8) is reduced to

$$F_{wind} = \frac{\rho_d}{N_J} e j n_e \tag{10}$$

Titanium has a density of 4.50 g/cm³, and an atomic weight of 47.867 g/mol, effective valence number $Z^* = 4$, and electrical resistivity of 1.78 μΩ.m [70]. From Eq. (9), its electron density/concentration is $n_e = 2.265 \times 10^{29}$ m⁻³.

Several authors have reported dislocation density in additively manufactured Ti–6Al–4V, and on the average, the dislocation density is of the order of $10^{14}~\text{m}^{-2}$ [71]. Thus, for a current density of $5\times10^5~\text{A/cm}^2$, the acting electron wind force per unit length of dislocation is

$$F_{wind} = \frac{\left(1.78 \times 10^{-6} \Omega.\text{m}\right)}{10^{14} \text{m}^{-2}} \left(1.6 \times 10^{-19} \text{ C}\right) \left(5 \times 10^{9} \text{ Am}^{-2}\right) \left(2.265 \times 10^{29} \text{ m}^{-3}\right)$$

$$F_{wind} = 3.23 \text{ N/m}$$

It is clear that the shear force per unit length due to the electron wind force is two orders of magnitude higher than critical shear force for causing twinning and one order of magnitude higher than critical shear force for initiating slip. In other words, electron wind force is capable of causing slip or twinning.

The results of the analysis of Schmid/Taylor factors in Figs. 6 and 7 can also be used to explain the increase in the nanohardness. In a modified strengthening model, the flow stress of a material can be expressed using Eq. (12) as a superposition of Taylor hardening [72] and Hall-Petch strengthening [73].

$$\sigma = \sigma_o + kMGbD^{-1/2} \tag{12}$$

where k is a constant, σ_0 is the intrinsic (friction) strength, M is the average Taylor factor, G is the shear modulus, b is the magnitude of the Burgers vector, and ρ is the dislocation density. By calculating the value of Schmid factor, m, for all orientations, the average Taylor factor, $M = \langle \frac{1}{m} \rangle$ can be determined as the average ensemble of the inverse of Schmid factors.

The Taylor factor is used to correlate the microscopic critical resolved shear stress (CRSS) to the macroscopic yield strength of the polycrystalline aggregate. It is also used to correlate he macroscopic and microscopic work hardening rates [74]. Thus, the Taylor factor depends on the crystallographic nature of the active slip systems at the grain level and by any orientation texture in the aggregate. Depending on the grain orientations with respect to the applied loading, not all slip systems will be activated (operative) for a particular slip system. Some of the grain with low to medium Taylor factor (soft slip systems) will rotate to undergo plastic deformation in appropriate slip systems, whereas some with high Taylor factor (low Schmid factor) will be difficult to rotate to activate slip and therefore develop high density of geometrically necessary dislocation (GND). Thus, for hcp polycrystalline aggregates, like Ti-6Al-4V, the bulk of the strain is normally accommodated by the soft slip systems, whereas the strength is controlled by the critical resolved shear stress (CRSS) of the hard systems [74,75].

Evidently, the higher values of Taylor factors for electric current processed specimen than for as-built specimen (Fig. 7) imply that the slip systems in the electric current processed specimen provide more resistance to yielding than the slip systems in the as-built condition, and therefore exhibit higher hardness. It should however be noted that for this analysis a threshold value of 0.2 was set as the minimum Schmid factor in the calculation of the Taylor factor [47]. The average Taylor factor \overline{M} is a contribution from the basal, prism, and pyramidal slip systems. However, since pyramidal slip system is very resistant to slip, and its critical resolved shear stress (CRSS) is reported to be about 7 times higher than that of basal slip system [47,51], it was omitted from the analysis.

Fig. 11 shows the pole figures and associated grain boundary misorientations of as-built (Fig. 11a & c) and after electric current

processing (Fig. 11b & d). It is clear from the pole figures that there is a discernible change in the crystal orientations due to electric current processing. The as-built specimen was populated with {0001} basal poles, with a high density of these poles tilted at about 35° from the build direction (BD). This tilt growth direction has been reported to be closely aligned with the maximum heat flow direction at the solid-liquid interface [76,77].

Interestingly, after electric current annealing the {0001} basal poles that were tilted from the BD retain their tilt, however they were noted to undergo a relative rotation of $\sim\!65^\circ$ about the BD. Also noted was an increase in the density of $\{11\overline{2}0\}//BD$ orientation.

It has been demonstrated that the room temperature (α -phase) texture of Ti-alloys stems from the high temperature β -phase [78–80]. This transformation is governed by the Burgers orientation relationship (BOR) such that the {0001} basal planes of the α phase are parallel to the {110} planes of the β phase, and the closed-packed <1120> directions of the α phase are parallel to the <111> directions of the β phase [81].

$$\{0001\}_{\alpha} \parallel \{110\}_{\beta} \text{ and } <1120>_{\alpha} \parallel <111>_{\beta}$$
 (13)

Based on this orientation relationship, the misorientations between neighboring α -variants fulfilling the BOR have been reported to be either 10.53° [0001] (*Type 6*), 60° [$11\overline{2}0$] (*Type 2*), 60.83° [$\overline{1.377}$ $\overline{1}$ 2.377 0.359] (*Type 3*), 63.26° [$\overline{10}$ 5 5 3] (*Type 4*), or 90° [1 $\overline{2.382}$ 1.38 0] (*Type 5*) [82,83].

The analysis of the boundary misorientations between neighboring (correlated) α -laths in the as-built specimen (Fig. 11c) conforms with the reported BOR and shows a strong peak at $\sim\!60^\circ$ (Type 3 & Type 4), a weak peak at 90° (Type 5) and marginal peaks at 10° (Type 6) and 30° . After electric current processing, there was a disappearance of the 30° boundaries, weakening of the 10° and 90° boundaries, and enhancement of the $\sim\!60^\circ$ boundaries (Fig. 11d). We can postulate that the high electron wind force causes local reorientation of the microstructure (α / α '-laths in this case) to orientations that are harder or more resistance to yield. Similar results have been reported by Kuang et al. [84] and Liu et al. [85]. This translates to a higher external applied stress to achieve yielding for electric current processed specimen than for the as-built specimen. This supports and is in agreement with the data on the nanohardness.

5. Conclusion

(11)

Producing strong and tough materials is the ultimate goal in materials development. Although conventional thermal annealing can be used to eliminate defects, it often leads to a drop in the mechanical properties. In this study we have presented a novel and economical method of healing defects by electric current processing, without compromising the mechanical properties.

We have demonstrated that with a proper electric current density generated during electric current processing, the athermal effects due to high electron wind force can provide "electro-strengthening" by reducing or eliminating defects with a corresponding improvement in the structural integrity. The results presented in this paper show that while the grain size increased by \sim 15%, the nanohardness increased by 16%. This is in contrast to the classical Hall-Petch behavior and is attributed to the pronounced reduction in defects and significant increase in the intrinsic strength as evidenced by the high Taylor factor of electric current processed specimen. We can postulate that the high electron wind force attracts and annihilates defects and cause local reorientation of the microstructure (α -laths in this case) to orientations that are harder or more resistance to yield. Thus, a higher external stress is required to initiate yielding in electric current processed specimen than the as-built specimen. Additionally, we have presented evidence that electric current processing also reduces residual stress present in asbuilt powder bed fusion additive manufacturing specimens.

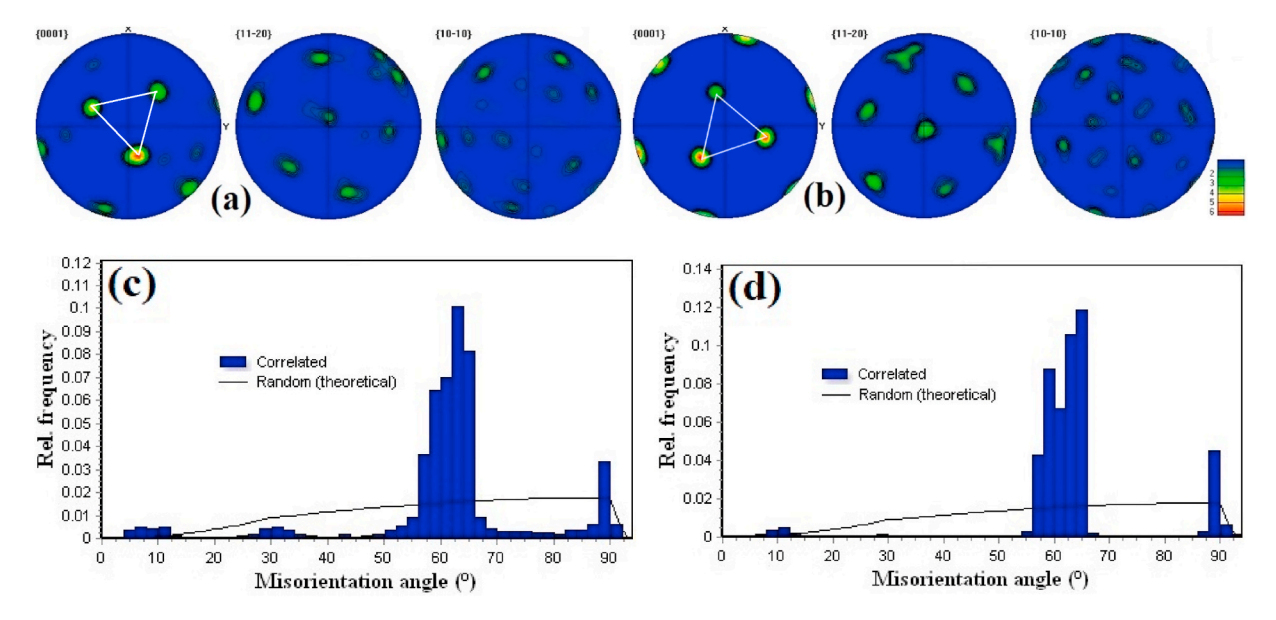


Fig. 11. Pole figures and associated grain boundary misorientations before (a, c) and after electric current processing (b, d).

Data availability

The raw/processed data required to reproduce these findings cannot be shared at this time as the data also forms part of an ongoing study.

Declaration of competing interest

The authors declare that they have no known competing financial interests or personal relationships that could have appeared to influence the work reported in this paper.

Acknowledgements

This work was supported by the National Science Foundation (Division of Civil, Mechanical, & Manufacturing Innovation, Nanomanufacturing program award # 1760931) and the U.S. Department of Energy funding (DE-NE0008259). Test coupon fabrication was performed at the Pennsylvania State University Center for Innovative Material Processing through Direct Digital Deposition (CIMP-3D) by the Applied Research Laboratory with support from the Naval Air Systems Command (NAVAIR) under Contract No. N00024-12-D-6404. Commonwealth Campuses Research Collaboration funding through the Office of the Vice President for Commonwealth Campuses (OVPCC) and Materials Research Institute (MRI, Pennsylvania State University, is also gratefully acknowledged. All characterization was performed at the Pennsylvania State University Materials Characterization Facility.

Appendix A. Supplementary data

Supplementary data to this article can be found online at https://doi.org/10.1016/j.msea.2020.140062.

References

- [1] M.L. Griffith, M.E. Schlienger, L.D. Harwell, M.S. Oliver, M.D. Baldwin, M.T. Ensz, M. Essien, J. Brooks, C.V. Robino, J.E. Smugeresky, W.H. Hofmeister, M.J. Wert, D. V. Nelson, Understanding the thermal behavior in the LENS process, Mater. Des. 20 (1999) 107–113.
- [2] B. Vrancken, L. Thijs, J.-P. Kruth, J. Van Humbeeck, Heat treatment of Ti6Al4V produced by selective laser melting: microstructure and mechanical properties, J. Alloys Compd. 541 (2012) 177–185.
- [3] H.K. Rafi, N.V. Karthik, H. Gong, T.L. Starr, B.E. Stucker, Microstructures and mechanical properties of Ti6Al4V parts fabricated by selective laser melting and electron beam melting, J. Mater. Eng. Perform. 22 (2013) 3872–3883.

- [4] B.E. Carroll, T.A. Palmer, A.M. Beese, Anisotropic tensile behavior of Ti-6Al-4V components fabricated with directed energy deposition additive manufacturing, Acta Mater. 87 (2015) 309–320.
- [5] D. Banerjee, J.C. Williams, Perspectives on titanium science and technology, Acta Mater. 61 (2013) 844–879.
- [6] X. Tan, Y. Kok, Y.J. Tan, M. Descoins, D. Mangelinck, S.B. Tor, K.F. Leong, C. K. Chua, Graded microstructure and mechanical properties of additive manufactured Ti-6Al-4V via electron beam melting, Acta Mater. 97 (2015) 1–16.
- [7] L.E. Murr, S.A. Quinones, S.M. Gaytan, M.I. Lopez, A. Rodela, E.Y. Martinez, D. H. Hernandez, E. Martinez, F. Medina, R.B. Wicker, Microstructure and mechanical behavior of Ti6Al4V produced by rapid-layer manufacturing, for biomedical applications, J. Mech. Behav. Biomed. Mater. 2 (2009) 20–32.
- [8] R. Boyer, G. Welsch, E.W. Collings, Materials Properties Handbook: Titanium Alloys, ASM International, 1994.
- [9] H. Gong, K. Rafi, H. Gu, G.D. Janaki Ram, T. Starr, B. Stucker, Influence of defects on mechanical properties of Ti-6Al-4V components produced by selective laser melting and electron beam melting, Mater. Des. 86 (2015) 545–554.
- [10] E. Wycisk, A. Solbach, S. Siddique, D. Herzog, F. Walther, C. Emmelmann, Effects of defects in laser additive manufactured Ti-6Al-4V on fatigue properties, Physics Procedia 56 (2014) 371–378.
- [11] T. Vilaro, C. Colin, J.D. Bartout, As-fabricated and heat-treated microstructures of the Ti6Al-4V alloy processed by selective laser melting, Metall. Mater. Trans. 42 (2011) 3190–3199.
- [12] C. Qiu, N.J.E. Adkins, M.M. Attallah, Selective laser melting of Invar 36: microstructure and properties, Acta Mater. 103 (2016) 382–395.
- [13] C. Kenel, D. Grolimund, X. Li, E. Panepucci, V.A. Samson, D. Ferreira Sanchez, F. Marone, C. Leinenbach, In-situ investigation of phase transformations in Ti-6Al-4V under additive manufacturing conditions combining laser melting and high speed micro-X-ray diffraction, Sci. Rep. 7 (2017) 16358, https://doi.org/10.1038/ s41598-017-16760-0.
- [14] A.A. Antonysamy, J. Meyer, P.B. Prangnell, Effect of build geometry on the β-grain structure and texture in additive manufacture of Ti6Al4V by selective electron beam melting, Mater. Char. 84 (2013) 153–168.
- [15] M. Simonelli, Y.Y. Tse, C. Tuck, Effect of the build orientation on the mechanical properties and fracture modes of SLM Ti-6Al-4V, Mater. Sci. Eng. A616 (2014) 1–11.
- [16] D.R. Waryoba, J.S. Keist, C. Ranger, T.A. Palmer, Microtexture in additively manufactured Ti-6Al-4V fabricated using directed energy deposition, Mater. Sci. Eng., A 734 (2018) 149–163.
- [17] A.S. Wu, D.W. Brown, M. Kumar, G.F. Gallegos, W.E. King, An experimental investigation into additive manufacturing induced residual stresses in 316L stainless steel, Metall. Mater. Trans. A45 (2014) 6260–6270.
- [18] X. Zhou, D. Wang, X. Liu, D. Zhang, S. Qu, J. Ma, G. London, Z. Shen, W. Liu, 3D-imaging of selective laser melting defects in a Co-Cr-Mo alloy by synchrotron radiation micro-CT, Acta Mater. 98 (2015) 1–16.
- [19] H. Gong, K. Rafi, H. Gu, T. Starr, B. Stucker, Analysis of defect generation in Ti–6Al–4V parts made using powder bed fusion additive manufacturing processes, Addit. Manuf. 1–4 (2014) 87–98.
- [20] S.T. Williams, H. Zhao, F. Léonard, F. Derguti, I. Todd, P.B. Prangnell, XCT analysis of the influence of melt strategies on defect population in Ti–6Al–4V components manufactured by Selective Electron Beam Melting, Mater. Char. 102 (2015) 47–61.
- [21] C. Qiu, N.J.E. Adkins, M.M. Attallah, Microstructure and tensile properties of selectively laser-melted and of HIPed laser-melted Ti–6Al–4V, Mater. Sci. Eng. A 578 (2013) 230–239.

- [22] M.-W. Wu, P.-H. Lai, The positive effect of hot isostatic pressing on improving the anisotropies of bending and impact properties in selective laser melted Ti-6Al-4V alloy, Mater. Sci. Eng. A 658 (2016) 429–438.
- [23] N. Chen, G. Ma, W. Zhu, A. Godfrey, Z. Shen, G. Wu, X. Huang, Enhancement of an additive-manufactured austenitic stainless steel by post-manufacture heattreatment, Mater. Sci. Eng. A 759 (2019) 65–69.
- [24] Z.Y. Zhao, L. Li, P.K. Bai, Y. Jin, L.Y. Wu, J. Li, R.G. Guan, H.Q. Qu, The heat treatment influence on the microstructure and hardness of TC4 titanium alloy manufactured via selective laser melting, Materials 11 (2018) 1318, https://doi. org/10.3390/ma11081318.
- [25] I.A. Blech, C. Herring, Stress generation by electromigration, Appl. Phys. Lett. 29 (1976) 131–133.
- [26] S.T. Pai, J.P. Marton, Electromigration in metals, Can. J. Phys. 55 (1977) 103-115.
- [27] A.K. Misra, A novel solidification technique of metals and alloys: under the influence of applied potential, Metall. Trans. 16A (1985) 1354–1355.
- [28] H. Conrad, Thermally activated plastic flow of metals and ceramics with an electric field or current, Mater. Sci. Eng., A 322 (2002) 100–107.
- [29] L. Guan, G. Tang, P.K. Chu, Recent advances and challenges in electroplastic manufacturing processing of metals, J. Mater. Res. 25 (2010) 1215–1224.
- [30] Y. Yuan, W. Liu, B. Fu, H. Xu, The effects of electropulsing on the recrystallization behavior of rolled pure tungsten, J. Mater. Res. 27 (2012) 2630–2638.
- [31] H. Guo, X. Zeng, J. Fan, H. Zhang, Q. Zhang, W. Li, H. Dong, B. Xu, Effect of electropulsing treatment on static recrystallization behavior of cold-rolled magnesium alloy ZK60 with different reductions, J. Mater. Sci. Technol. 35 (2019) 1113–1120.
- [32] Z. Islam, H. Gao, A. Haque, Synergy of elastic strain energy and electron wind force on thin film grain growth at room temperature, Mater. Char. 152 (2019) 85–93.
- [33] D. Waryoba, Z. Islam, B. Wang, A. Haque, Low temperature annealing of metals with electrical wind force effects, J. Mater. Sci. Technol. 35 (2019) 465–472.
- [34] Y. Jiang, G. Tang, C. Shek, W. Liu, Microstructure and texture evolution of the coldrolled AZ91 magnesium alloy strip under electropulsing treatment, J. Alloys Compd. 509 (2011) 4308–4313.
- [35] S.-J. Kim, S.-D. Kim, D. Yoo, J. Lee, Y. Rhyim, D. Kim, Evaluation of the athermal effect of electric pulsing on the recovery behavior of magnesium alloy, Metall. Mater. Trans. 47A (2016) 6368–6373.
- [36] H.J. Jeong, M.J. Kim, J.W. Park, C.D. Yim, J.J. Kim, O.D. Kwon, P.P. Madakashira, H.N. Han, Effect of pulsed electric current on dissolution of Mg17Al12 phases in asextruded AZ91 magnesium alloy, Mater. Sci. Eng. A 684 (2017) 668–676.
- [37] Y.H. Zhu, S. To, W.B. Lee, X. Liu, Y. Jiang, G. Tang, Electropulsing-induced phase transformations in a Zn-Al-based alloy, J. Mater. Res. 24 (2011) 2661–2669.
- [38] F. Wang, D. Huo, S. Li, Q. Fan, Inducing TiAl3 in titanium alloys by electric pulse heat treatment improves mechanical properties, J. Alloys Compd. 550 (2013) 133–136.
- [39] L. Pan, W. He, B. Gu, Non-uniform carbon segregation induced by electric current pulse under residual stresses. J. Mater. Process. Technol. 226 (2015) 247–254.
- [40] R.S. Qin, Y.K. Luo, B. E-Bowman, O. Omoigiade, Fabrication of nanostructured pearlite steel wires using electropulsing, Mater. Sci. Technol. 14 (2017) 1–6.
- [41] H. Song, Z.J. Wang, Microcrack healing and local recrystallization in pre-deformed sheet by high density electropulsing, Mater. Sci. Eng. A 490 (2008) 1–6.
- [42] T. Yu, D. Deng, G. Wang, H. Zhang, Crack healing in SUS304 stainless steel by electropulsing treatment, J. Clean. Prod. 113 (2016) 989–994.
- [43] Y. Sheng, Y. Hua, X. Wang, X. Zhao, L. Chen, H. Zhou, J. Wang, C.C. Berndt, W. Li, Application of high-density electropulsing to improve the performance of metallic materials: mechanisms, microstructure and properties, Materials 11 (2018) 185, https://doi.org/10.3390/ma11020185.
- [44] C. Basaran, M. Lin, Damage mechanics of electromigration induced failure, Mech. Mater. 40 (2008) 66–79.
- [45] A.C. Fischer-Cripps, Nanoindentation, third ed., Springer-Verlag, New York, 2011.
- [46] W.C. Oliver, G.M. Pharr, An improved technique for determining hardness and elastic modulus using load and displacement sensing indentation experiments, J. Mater. Res. 7 (1992) 1564–1583.
- [47] H. Li, D.E. Mason, T.R. Bieler, C.J. Boehlert, M.A. Crimp, Methodology for estimating the critical resolved shear stress ratios of α-phase Ti using EBSD-based trace analysis, Acta Mater. 61 (2013) 7555–7567.
- [48] X. Wu, S.R. Kalidindi, C. Necker, A.A. Salem, Prediction of crystallographic texture evolution and anisotropic stress-strain curves during large plastic strains in high purity α-titanium using a Taylor-type crystal plasticity model, Acta Mater. 55 (2007) 423–432.
- [49] Y. Yang, L. Wang, T.R. Bieler, P. Eisenlohr, M.A. Crimp, Quantitative atomic force microscopy characterization and crystal plasticity finite element modeling of heterogeneous deformation in commercial purity titanium, Metall. Mater. Trans. 42 (2011) 636–644.
- [50] H. Li, D.E. Mason, Y. Yang, T.R. Bieler, M.A. Crimp, C.J. Boehlert, Comparison of the deformation behavior of commercially pure titanium and Ti-5Al-2.5Sn(wt.%) at 296 and 728 K, Philos. Mag. A 93 (2013) 2875–2895.
- [51] R.A. Lebensohn, G.R. Canova Gr, A self-consistent approach for modelling texture development of two-phase polycrystals: application to titanium alloys, Acta Mater. 45 (1997) 3687–3694.
- [52] J.-W. Park, H.-J. Jeong, S.-W. Jin, M.-J. Kim, K. Lee, J.J. Kim, S.-T. Hong, H.N. Han, Effect of electric current on recrystallization kinetics in interstitial free steel and AZ31 magnesium alloy, Mater. Char. 133 (2017) 70–76.
- [53] N. Kamikawa, X. Huang, N. Tsuji, N. Hansen, Strengthening mechanisms in nanostructured high-purity aluminum deformed to high strain and annealed, Acta Mater. 57 (2009) 4198–4208.

- [54] X. Huang, N. Hansen, N. Tsuji, Hardening by annealing and softening by deformation in nanostructured metals, Science 312 (2006) 249–251.
- [55] J.P. Hirth, Theory of Dislocations, second ed., Wiley, New York, 1982.
- [56] W. Li, Y. Shen, C. Xie, Effect of electric pulses on annealing hardening of submicro metre grained copper, Mater. Sci. Technol. 31 (2015) 1577–1582.
- [57] Z.-J. Wang, Q.-J. Li, Y.-N. Cui, Z.-L. Liu, E. Ma, J. Li, J. Sun, Z. Zhuang, M. Dao, Z.-W. Shan, S. Suresh, Cyclic deformation leads to defect healing and strengthening of small-volume metal crystals, Proc. Natl. Acad. Sci. USA 112 (2015) 13502–13507.
- [58] E.M. Lehockey, Y.-P. Lin, O.E. Lepik, Mapping residual plastic strain in materials using electron backscatter diffraction, in: A.J. Schwartz, M. Kumar, B.L. Adams (Eds.), Electron Backscatter Diffraction in Materials Science, Springer, Boston, MA, 2000, pp. 247–264.
- [59] M. Kamaya, A.J. Wilkinson, J.M. Titchmarsh, Quantification of plastic strain of stainless steel and nickel alloy by electron backscatter diffraction, Acta Mater. 2 (2006) 539–548.
- [60] Z. Islam, B. Wang, A. Haque, Current density effects on the microstructure of zirconium thin films, Scripta Mater. 144 (2018) 18–21.
- [61] S. Plimpton, Fast parallel algorithms for short-range molecular-dynamics, J. Comput. Phys. 117 (1995) 1–19.
- [62] G. Bonny D. Terentyev, R.C. Pasianot, S. Poncé, A. Bakaev, Interatomic potential to study plasticity in stainless steels: the FeNiCr model alloy, Model. Simulat. Mater. Sci. Eng. 19 (2011).
- [63] R.R. Zope, Y. Mishin, Interatomic potentials for atomistic simulations of the Ti-Al system, Phys. Rev. B 68 (2003), 024102.
- [64] R.S. Sorbello, A. Lodder, S.J. Hoving, Finite-cluster description of electromigration, Phys. Rev. B Condens. Matter 25 (1982) 6178–6187.
- [65] X. Wu, S.R. Kalidindi, C. Necker, A.A. Salem, Prediction of crystallographic texture evolution and anisotropic stress–strain curves during large plastic strains in high purity α-titanium using a Taylor-type crystal plasticity model, Acta Mater. 55 (2007) 423–432.
- [66] I.J. Beyerlein, J. Wang, M.R. Barnett, C.N. Tomé, Double twinning mechanisms in magnesium alloys via dissociation of lattice dislocations, Proc. R. Soc. A 468 (2012) 1496–1520, https://doi.org/10.1098/rspa.2011.0731.
- [67] B.W. Levinger, Lattice parameter of beta titanium at room temperature, transactions AIME, J. Metals 5 (1953) 195, https://doi.org/10.1007/BF03397474.
- [68] M. Peach, J.S. Koehler, The forces exerted on dislocations and the stress fields produced by them, Phys. Rev. 80 (1950) 436–439.
- [69] H. Conrad, A.F. Sprecher, W.O. Cao, X.P. Lu, Electroplasticity the Effect of electricity on the mechanical properties of metals, JOM (J. Occup. Med.) 42 (1990) 28–33.
- [70] L. Bolzoni, E.M. Ruiz-Navas, E. Gordo, Flexural properties, thermal conductivity and electrical resistivity of prealloyed and master alloy addition powder metallurgy Ti-6Al-4V, Mater. Des. 52 (2013) 888–895.
- [71] S. Gorsse, C. Hutchinson, M. Gouné, R. Banerjee, Additive manufacturing of metals: a brief review of the characteristic microstructures and properties of steels, Ti-6Al-4V and high-entropy alloys, Sci. Technol. Adv. Mater. 18 (2017) 584–610.
- [72] G.I. Taylor, The mechanism of plastic deformation of crystals: Part I Theoretical, Proc. Roy. Soc. Lond. 145 (1934) 362–387.
- [73] N. Hansen, Hall-Petch relation and boundary strengthening, Scripta Mater. 51 (2004) 801–806.
- [74] U.F. Kocks, H. Mecking, Physics and phenomenology of strain hardening: the FCC case, Prog. Mater. Sci. 48 (2003) 171–273.
- [75] A. Couret, D. Caillard, Microscopic observations of glide in non close-packed planes in aluminum, and comparison with magnesium, Acta Metall. 36 (1988) 2515–2524.
- [76] O. Zinovieva, A. Zinoviev, V. Ploshikhin, Three-dimensional modeling of the microstructure evolution during metal additive manufacturing, Comput. Mater. Sci. 141 (2018) 207–220.
- [77] T. DebRoy, H.L. Wei, J.S. Zuback, T. Mukherjee, J.W. Elmer, J.O. Milewski, A. M. Beese, A. Wilson-Heid, A. De, W. Zhang, Additive manufacturing of metallic components process, structure and properties, Prog. Mater. Sci. 92 (2018) 112–224.
- [78] I. Lonardelli, N. Gey, H.-R. Wenk, M. Humbert, S.C. Vogel, L. Lutterotti, In situ observation of texture evolution during $\alpha \rightarrow \beta$ and $\beta \rightarrow \alpha$ phase transformations in titanium alloys investigated by neutron diffraction, Acta Mater. 55 (2007) 5718–5727.
- [79] G.G.E. Seward, S. Celotto, D.J. Prior, J. Wheeler, R.C. Pond, In situ SEM-EBSD observations of the hcp to bcc phase transformation in commercially pure titanium, Acta Mater. 52 (2004) 821–832.
- [80] S.C. Wang, M. Aindow, M.J. Starink, Effect of self-accommodation on α-α boundary populations in pure titanium, Acta Mater. 51 (2003) 2485–2503.
- [81] W.G. Burgers, On the process of transition of the cubic-body-centered modification into the hexagonal-close-packed modification of zirconium, Physica 1 (1934) 561–586
- [82] T. Karthikeyan, S. Saroja, M. Vijayalakshmi, Evaluation of misorientation angleaxis set between variants during transformation of BCC to HCP phase obeying Burgers orientation relationship, Scripta Mater. 5 (2006) 771–774.
- [83] N. Gey, M. Humbert, Specific analysis of EBSD data to study the texture inheritance due to the $\beta \to \alpha$ phase transformation, J. Mater. Sci. 38 (2003) 1289–1294.
- [84] J. Kuang, X. Du, X. Li, Y. Yang, A.A. Luo, G. Tang, Athermal influence of pulsed electric current on the twinning behavior of Mg-3Al-1Zn alloy during rolling, Scripta Mater. 114 (2016) 151-155.
- [85] Y.-C. Liu, S.-K. Lin, S.-J. Chiu, On the Schmid's Law for the electric current-induced deformation: an in situ EBSD study, Int. J. Mech. Sci. 168 (2020) 105295.